 Research Article

OPTICA QUANTUM

Spatio-spectral quantum state estimation of photon pairs from optical fiber using stimulated emission

DONG BEOM KIM,[1,2,*] XIYE HU,[1,2] ALFRED B. U'REN,[3] KARINA GARAY-PALMETT,[4] AND VIRGINIA O. LORENZ[1,2]

[1] Department of Physics, University of Illinois Urbana-Champaign, Urbana, Illinois 61801, USA
[2] Illinois Quantum Information Science & Technology Center (IQUIST), University of Illinois Urbana-Champaign, Urbana, Illinois 61801, USA
[3] Instituto de Ciencias Nucleares, Universidad Nacional Autónoma de México, A.P. 70-543, 04510 Ciudad de México, Mexico
[4] Departamento de Óptica, Centro de Investigación Científica y de Educación Superior de Ensenada, B.C., 22860, Ensenada, Mexico
*dbkim3@illinois.edu

Received 3 December 2024; revised 17 March 2025; accepted 22 April 2025; published 7 May 2025

Developing a quantum light source that carries more than one bit per photon is pivotal for expanding quantum information applications. Characterizing a high-dimensional multiple-degree-of-freedom source at the single-photon level is challenging due to the large parameter space as well as limited emission rates and detection efficiencies. Here, we characterize photon pairs generated in optical fiber in the transverse-mode and frequency degrees of freedom by applying stimulated emission in both degrees of freedom while detecting in one of them at a time. This method may be useful in the quantum state estimation and optimization of various photon-pair source platforms in which complicated correlations across multiple degrees of freedom may be present.

https://doi.org/10.1364/OPTICAQ.547491

1. INTRODUCTION

Developing an efficient quantum light source [1–3] that can carry more than one bit of information per photon is crucial for expanding quantum information applications in communication [4,5], computation [6], and metrology [7–9]. Optical fiber-based photon-pair sources [1] are an attractive platform that promise3s easy integration with existing fiber networks and correlations across multiple high-dimensional degrees of freedom (DOF) such as time, frequency, and transverse spatial mode [10–12].

Nevertheless, exploiting such multi-dimensionality requires non-trivial state characterization [1,13,14]. This characterization can be challenging to implement with conventional spontaneous-emission measurements including quantum state tomography (QST) [15]. The detection needs to span the entire multi-DOF space [10,16,17], potentially aided by extended QST methods such as adaptive quantum state tomography [18,19], self-guided tomography [17,20], and compressed sensing [21,22]. Moreover, the coincidence-counting measurements involved often require single-photon sensitivity [23,24], long integration times [10,12], and a large number of projective measurements [16,17].

Stimulated-emission tomography (SET) [14,25–27] can speed up characterization through both stimulation and detection in multiple DOFs. The measurements employ classical seed light that stimulates the photon-pair generation process. The higher count rates of the stimulated process lead to more efficient tomography [25]. These stimulated measurements have previously been applied to a single DOF, such as polarization [27], frequency [25,26,28], and transverse spatial mode [29–32], and multiple DOFs including polarization-frequency [14], and polarization-path [33].

In this work, we extend this effort to introduce a multi-dimensional characterization method that can be applied to sources with correlations in multiple high-dimensional DOFs, in particular transverse spatial mode and frequency. We utilize a few-mode polarization-maintaining fiber source that produces photon pairs correlated in transverse mode and frequency via spontaneous four-wave mixing (SFWM) [10–12]. We implement stimulated emission in multiple DOFs (transverse mode and frequency), but detect in one DOF at a time (transverse mode or frequency) [34]. See Fig. 1 for a graphical representation of the overall experimental concept. We use a seed beam shaped in transverse mode and frequency [29,35–37] to stimulate the four-wave mixing (FWM) process, and measure the transverse-mode images and spectra of the stimulated signal using a camera and a spectrometer. Because the transverse modes and spectral modes are correlated, transverse-mode-resolved joint spectral intensities (JSIs)—an *inter*-DOF—can be used to investigate the transverse-mode quantum state—intra-DOF—of the photon pairs. The acquired *inter*-DOF coherence information can thus yield the intra-DOF coherence information.

This method reduces the number of measurements while still providing the coherence information across multiple DOFs. Our result also shows that stimulated-emission imaging [29,31] can be achieved in fiber platforms, exhibiting a real-time monitoring capability. Consequently, this method can be used in conjunction with quantum state tomography to estimate the quantum state and diagnose the underlying causes of deviations from the target state in each DOF. Our method of extracting multi-dimensional information via stimulated emission using detection in one DOF can immediately aid in optimizing various photon-pair source platforms [1,6,38–42] where complicated correlations arise across multiple DOFs and generation processes.

2. THEORY

2.1. Transverse Spatial Modes in Few-Mode PMF

Linearly polarized modes are the transverse spatial modes supported in a conventional cylindrically symmetric optical fiber that satisfies the weakly guided approximation [43]. These modes are denoted as LP_{lmq}, where l, m, and q are the azimuthal, radial, and parity indices describing their modal structures [11,43]. In this paper, we consider a few-mode PMF that supports three LP modes: $|LP_{01}\rangle = |g\rangle$, $|LP_{11e}\rangle = |e\rangle$, and $|LP_{11o}\rangle = |o\rangle$ [see Fig. 1(a)]. As transverse-mode basis states, these three LP modes can be combined to form superposition states, e.g., $|d, a\rangle = (|e\rangle \pm |o\rangle)/\sqrt{2}$ and $|r, l\rangle = (|e\rangle \pm i|o\rangle)/\sqrt{2}$ as shown in Fig. 1(a). The modes are then further affected by the two types of birefringence in the PMF: a polarization birefringence $\Delta = n^x - n^y$ between the slow (x) and fast (y) axes of the PMF and a parity birefringence $\Delta^p = n^o - n^e$ between transverse modes with even (e) and odd (o) parities. Figure 1 shows how the slow (x) axis of the PMF is oriented along the vertical direction and the mode $|e\rangle$ intensity lobes.

When characterizing the photon-pair generation process in a few-mode PMF, it is important to accurately describe the property of a transverse mode at a given wavelength. For this purpose, we define an effective refractive index, which takes into account the transverse geometrical effect of the optical fiber (T_ν) as well as its material dispersion property (ω_ν): $n_\nu^{T_\nu} = n_{\text{eff}}(\omega_\nu, T_\nu)$, where ν indicates pump p, signal s, or idler i; and T_ν and ω_ν indicate transverse mode and frequency, respectively. Using this convention in the xx–yy cross-polarized scheme [11,44], in which the pump is polarized along x and the signal and idler are polarized along y, the effective refractive indices of the $|e\rangle$ and $|o\rangle$ modes can be represented as the following: $n_p^{ex} = n_p^e + \Delta$, $n_p^{ox} = n_p^{ex} + \Delta^p$, $n_{s,i}^{ey} = n_{s,i}^e$, and $n_{s,i}^{oy} = n_{s,i}^{ey} + \Delta^p$.

2.2. Four-Wave Mixing in Few-Mode PMF

Utilizing the transverse modes, the few-mode PMF can generate photon pairs correlated in transverse mode and frequency [10–12] through a nonlinear optical process called SFWM [45]. The SFWM process relies on the $\chi^{(3)}$ nonlinear optical susceptibility of the fiber to annihilate two pump photons (p_1, p_2) and create a signal (s) and an idler (i) photon pair. For this nonlinear process to occur, it needs to satisfy a phase-matching condition, which is determined by the energy ($\Delta\omega = 0$) and momentum conservation ($\Delta k = 0$) constraints, with

$$\begin{aligned}\Delta\omega &= \omega_{p_1} + \omega_{p_2} - \omega_s - \omega_i,\\ \Delta k &= k_{p_1} + k_{p_2} - k_s - k_i - k_{NL}\\ &= n(\omega_{p_1}, T_{p_1})\frac{\omega_{p_1}}{c} + n(\omega_{p_2}, T_{p_2})\frac{\omega_{p_2}}{c}\\ &\quad - n(\omega_s, T_s)\frac{\omega_s}{c} - n(\omega_i, T_i)\frac{\omega_i}{c} - k_{NL},\end{aligned} \tag{1}$$

where ω_ν, T_ν, k_ν are the angular frequency, transverse mode, and wavenumber, respectively, of $\nu = \{p_1, p_2, s, i\}$, c is the speed of light, and k_{NL} is the nonlinear contribution from self- and cross-phase modulation [44]. Among the different types of SFWM that Eq. (1) can represent, in this paper, we concentrate on the xx–yy cross-polarized birefringent phase-matching with frequency-degenerate pumps ($\omega_p = \omega_{p_1} = \omega_{p2}$) to take advantage of the reduced Raman scattering noise and the number of possible SFWM processes [44,46,47]. Additionally, since the effective refractive index $n(\omega_\nu, T_\nu)$ depends on the transverse mode (T_ν) and frequency (ω_ν), the phase-matching condition in Eq. (1) will vary for different combinations of the two. This can lead to photon pairs in different transverse modes acquiring dissimilar frequencies as shall be shown in Section 4.

2.3. Quantum State Representation of Photon Pairs

With the fundamentals of the transverse modes and SFWM introduced, we can now express the quantum state $|\psi_{si}\rangle$ of the photon pair created from the few-mode PMF. Assuming cross-polarized birefringent phase-matching and frequency-degenerate pumps, the signal–idler photon pair $|\psi_{si}\rangle$ can be generated in a superposition of N distinct SFWM processes as

$$|\psi_{si}\rangle = \sum_j^N \int \mathrm{d}\omega_s\, \mathrm{d}\omega_i\, c_j |\omega_s\omega_i, T_sT_i, yy, \ldots\rangle_j = \sum_j^N C_j \otimes |T_sT_i\rangle_j, \tag{2}$$

where the prefactors weighting each process j are

$$\begin{aligned}c_j &= M_{cj}\sqrt{P_{p_1j}P_{p_2j}}\, f_j(\omega_s, \omega_i) O_j(T_{p_1}, T_{p_2}, T_s, T_i),\\ C_j &= \int \mathrm{d}\omega_s\, \mathrm{d}\omega_i\, c_j |\omega_s\omega_i, yy, \ldots\rangle_j.\end{aligned} \tag{3}$$

Here, $|\omega_s\omega_i, T_sT_i, yy, \ldots\rangle_j$ represents the signal–idler state from SFWM process j in transverse mode, frequency, polarization, and other implicit degrees of freedom, e.g., position, time, etc. This expression is simplified as $C_j \otimes |T_sT_i\rangle_j$ to highlight the transverse-mode contribution. The prefactors c_j and C_j, which determine the relative amplitude and phase of each SFWM process j, are functions of average pump power $P_{p_{1,2}j}$, joint spectral amplitude (JSA) $f_j(\omega_s, \omega_i)$, and transverse-mode overlap integral $O_j(T_{p_1}, T_{p_2}, T_s, T_i)$. Here O_j quantifies the spatial overlap of the four transverse modes participating as defined in Ref. [11]. Here M_{cj} is the normalization constant satisfying $\langle\psi_{si}|\psi_{si}\rangle = 1$.

The JSA $f_j(\omega_s, \omega_i)$, which contains information about spectral correlations between signal and idler photons for each SFWM process [1,10–13,48], is defined and linearly approximated as [44]

$$\begin{aligned}f_j(\omega_s, \omega_i) &= \int \mathrm{d}\omega_p\, \alpha(\omega_p)\alpha(\omega_s + \omega_i - \omega_p)\phi_j(\omega_s, \omega_i)\\ &\approx \alpha(\omega_s, \omega_i)\phi_j(\omega_s, \omega_i),\end{aligned} \tag{4}$$

where $\alpha(\omega_s, \omega_i)$ is the pump spectral envelope function and $\phi_j(\omega_s, \omega_i)$ is the phase-matching function specific for j. For degenerate pumps, the JSA can be linearly approximated to $f_j(\omega_s, \omega_i) \approx \alpha(\omega_s, \omega_i)\, \mathrm{sinc}(\frac{L}{2}\Delta k_j)e^{i\frac{L}{2}\Delta k_j}$ where L is the length of the fiber and Δk_j is the phase mismatch for the process j as defined in Eq. (1). For non-degenerate pumps, while the JSA can be linearly approximated in the same form as Eq. (4), it is also a function of the temporal walk-off between the two pumps [49,50]. In our system, $\alpha(\omega_s, \omega_i)$ and $\phi_j(\omega_s, \omega_i)$ determine the spectral widths of the JSA peak along the diagonal and anti-diagonal directions, respectively. In this paper, we measure the JSI $|f_j(\omega_s, \omega_i)|^2$. The joint spectral phase (JSP) is defined

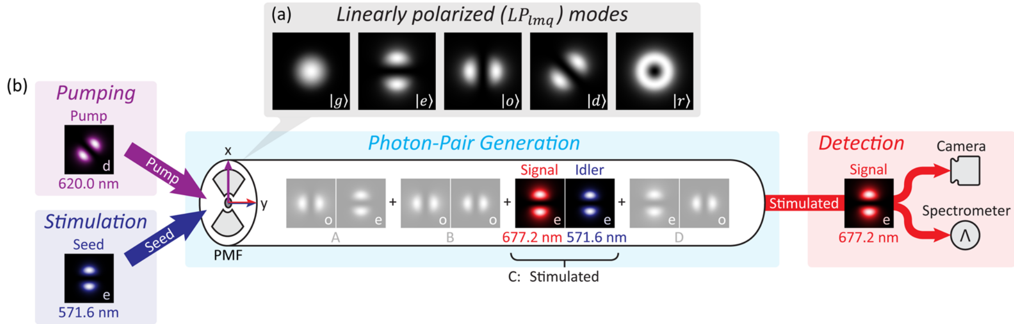

Fig. 1. Experimental concept. (a) Intensity distributions of three linearly polarized (LP) modes supported in polarization-maintaining fiber (PMF), $|g = LP_{01}\rangle$, $|e = LP_{11e}\rangle$, and $|o = LP_{11o}\rangle$, and two modes in superposition, $|d\rangle = (|e\rangle + |o\rangle)/\sqrt{2}$ and $|r\rangle = (|e\rangle + i|o\rangle)/\sqrt{2}$. (b) In our experiment, pump and seed (= idler) in a particular spatiospectral combination stimulate the generation of signal–idler photon pairs in specific modes (indicated with braces) among all observable spontaneous four-wave mixing processes labeled A–D (faded out in gray). The stimulated signal photons are measured with a camera or a spectrometer and used to estimate the quantum state of the signal–idler photon pairs.

as $\arg\{f_j(\omega_s, \omega_i)\}$. See Supplement 1 for a more comprehensive explanation of the factors in Eq. (3) and the quantum state representation of the pump.

The fiber parameters for the PMF considered here (Fibercore HB800C) are obtained through genetic algorithm analysis [10] to be: fiber core radius $r = 1.74\,\mu\text{m}$, numerical aperture $NA = 0.17$, $\Delta = 2.37 \times 10^{-4}$, $\Delta^p = 4.41 \times 10^{-4}$. With these parameters and the three transverse modes ($|g\rangle$, $|e\rangle$, and $|o\rangle$) for the pump, signal, and idler, only 10 out of 15 SFWM processes satisfy orbital angular momentum (OAM) and parity conservation and therefore are experimentally realizable [10,11]. Considering only the $|e\rangle$ and $|o\rangle$ modes, five of the above SFWM processes are viable with the following transverse mode combinations $\left(T_{p_1}, T_{p_2}, T_s, T_i\right)$: A (e, o, o, e), B (o, o, o, o), C (e, e, e, e), D (e, o, e, o), and E (o, o, e, e), where the labels A–E will be used throughout the paper to indicate the corresponding processes.

Using the formalism introduced earlier in Eqs. (2) and (3), these five FWM processes can be obtained with the two pumps in superpositions of $|e\rangle$ and $|o\rangle$ transverse modes, i.e., $|\psi_p\rangle = |\psi_{p_1}\rangle = |\psi_{p_2}\rangle = A_e|e_p\rangle + A_o|o_p\rangle$ given that we do not have individual control over the two pumps. The quantum states of the pumps $|\psi_{p_1p_2}\rangle$ and the signal–idler photon pairs $|\psi_{si}\rangle$ can be represented as

$$\begin{aligned} |\psi_{p_1p_2}\rangle &= |\psi_p\rangle^{\otimes 2} = B_{ee}|e_{p_1}e_{p_2}\rangle + 2B_{eo}|e_{p_1}o_{p_2}\rangle + B_{oo}|o_{p_1}o_{p_2}\rangle, \\ |\psi_{si}\rangle &= C_{ee}|e_s e_i\rangle + C_{eo}|e_s o_i\rangle + C_{oe}|o_s e_i\rangle + C_{oo}|o_s o_i\rangle, \end{aligned} \tag{5}$$

where A_j and B_j are prefactors similar to C_j (see Supplement 1 for details; these are different from the FWM process labels, A, B, and C). Here, $\otimes$ between A_j, B_j, C_j, and $|\cdots\rangle_j$ are omitted for simplicity. Notice that $B_{eo}|e_{p_1}o_{p_2}\rangle = B_{oe}|o_{p_1}e_{p_2}\rangle$ is satisfied due to their indistinguishability, resulting in an extra factor of 2 before the B_{eo} pump term and the corresponding C_{eo} and C_{oe} signal–idler terms, implicitly through $P_{p_{1,2}j}$ in Eq. (3).

Stimulated emission provides an efficient way to characterize the state in Eq. (5) using either the signal or idler as a seed. By controlling the transverse modes and frequencies of the pump and the seed (idler), individual FWM process(es), and thus the photon-pair state in Eq. (5) can be selectively excited [see Fig. 1(b)]. This is equivalent to applying a projection operator $|\omega_i, T_i, y\rangle_{j_0}\langle\omega_i, T_i, y|_{j_0}$, which describes the idler of process j_0, to $|\psi_{si}\rangle$ in Eq. (5) to obtain the stimulated photon state $|\omega_s, T_s, y\rangle_{j_0}$. This process is highly efficient [14,34] when used in conjunction with a classical seed beam since the stimulated photon number is linearly proportional to the seed photon number [25,26]. This requires sufficiently well-defined pump (T_{p_1}, T_{p_2}) and seed (T_i) transverse modes as well as a narrow spectral bandwidth seed (ω_i), as will become clear in the following sections.

3. METHODS

We use the experimental setup shown in Fig. 2 to characterize our fiber-based photon-pair source in both transverse mode and wavelength via stimulated emission. An optical parametric oscillator (OPO) (Inspire HF100) generates a pump beam with ≈ 200 fs pulse width, 80 MHz repetition rate, 8 mW average beam power, and 620 nm center wavelength. We couple this pump into a 10 cm-long few-mode PMF (HB800C, Fibercore) with its polarization along the slow axis (x) for cross-polarized SFWM photon-pair generation as described in Section 2. A continuous wave (CW) ring dye laser (Coherent 899) generates a classical seeded idler beam with narrow 2 GHz linewidth and 2 mW average beam power that is wavelength-tunable around 570 nm. We couple this seed beam into the same PMF with its polarization along the fast axis (y) to stimulate the FWM processes.

In order to selectively excite and stimulate specific FWM processes, it is crucial that we precisely control the spatial, spectral, and polarization states of the pump and the seed. We employ reflective phase-only spatial light modulators (SLM) (Holoeye Pluto 2), seed laser wavelength calibration with a spectrometer (Andor SR303i with iDus 420), and polarization optics to control the respective DOF. Spatially, we use the SLMs to shape the pump [51] to $|d\rangle$ and the seed to $|e\rangle$, $|o\rangle$, and $|d\rangle$ for Section 4. In addition to the standard transverse-mode control techniques involving computer-generated SLM phase masks [23,35–37,52,53], we adjust the phase mask iteratively until only one FWM process (spectral peak) is observed at a time in the spontaneous or stimulated FWM spectrum. Spectrally, we calibrate the seed laser wavelength scan with a spectrometer (see Supplement 1 for the calibration result). The interference filters spectrally shape the pump to approximately 2 nm full-width at half-maximum (FWHM) centered around 620 nm and filter the stimulated signal to a broad (670 to 700 nm) range or a narrow ~ 1 nm FWHM range depending on the application. Other optics including wave plates, linear polarizers,

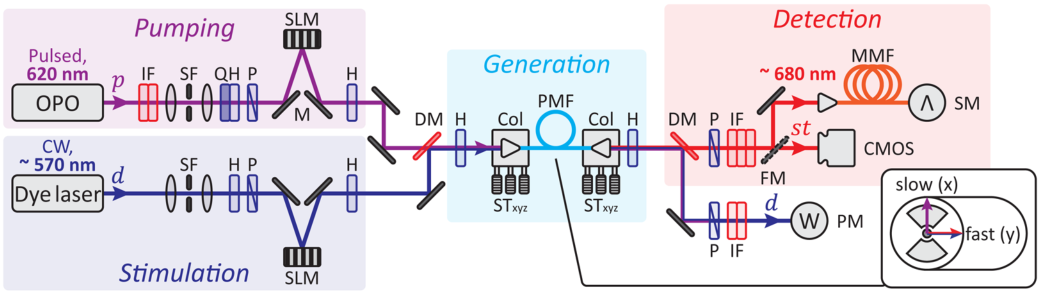

Fig. 2. Experimental setup. Spatiospectrally structured pump and seed beams stimulate a particular photon-pair state in optical fiber that is further detected with a spectrometer or a CMOS camera. The inset shows the slow (x) and fast (y) axes of the PMF. Here p, pump; d, seed; st, stimulated signal; IF, interference filter; SF, spatial filter consisting of a pinhole and a convex lens pair; Q, quarter-wave plate; H, half-wave plate; P, linear polarizer; M, mirror; SLM, spatial light modulator; DM, dichroic mirror; Col, collimator; $\mathrm{ST_{xyz}}$, xyz-translation stage; PMF, polarization-maintaining fiber; FM, flip mirror; SM (Λ), spectrometer; PM (W), power meter.

and pinhole spatial filters supplement the beam preparation for accurate FWM process excitation.

For a full characterization of all the FWM processes, we scan the seed wavelength in the (567 to 576 nm) range in steps of 0.05 nm. For a given seed wavelength, these stimulated photons are measured in two degrees of freedom, switchable via a flip mirror: wavelength with a spectrometer and transverse mode with a CMOS camera (Thorlabs CS505MU) using 16 px × 16 px pixel binning. A power meter at the PMF output normalizes the measured data with the seed power. These spectral and spatial data are then used to reconstruct the JSI [26] and resolve the corresponding transverse-mode state, respectively, i.e., transverse-mode-resolved JSI.

4. RESULTS

4.1. Transverse-Mode-Resolved JSI

Using the methods described in Section 3, we measure transverse-mode-resolved JSIs. Figure 3 shows the measured JSI plots of the photon pairs and the transverse-mode images of the stimulated signal photons. The signal transverse modes are imaged with exposure times of 200 ms for Figs. 3(a) and 3(b) and 400 ms for Fig. 3(c). Narrow signal spectral filters (~ 1 nm FWHM) are used to isolate individual FWM processes. Note that the states of the stimulated signal (st) and the seed (d) will reflect those of the spontaneously generated signal (s, around 680 nm) and the idler (i, around 570 nm) photons, respectively.

We vary the seed transverse modes to $|e\rangle$, $|o\rangle$, and $|d\rangle$ [see Figs. 3(a)–3(c)] while keeping the pump mode at $|d\rangle = (|e\rangle + |o\rangle)/\sqrt{2}$. This choice of seed transverse mode as well as its wavelength changes the JSI and the stimulated signal transverse mode, which helps isolate different FWM processes. Specifically, only the FWM processes that involve the given idler (seed) transverse mode and wavelength manifest in the JSI plot and the signal images. For example, with $|e\rangle$ ($|o\rangle$) seed and $|d\rangle$ pump, only the A and C (B and D) processes are stimulated, as shown in Fig. 3(a) [Fig. 3(b)]. On the other hand, with the seed in superposition state $|d\rangle$, all of the four FWM processes are stimulated, as shown in Fig. 3(c) (process E is outside our spectral range of interest and expected to appear at $(\lambda_s, \lambda_i)_E \sim (730, 540)_E$ nm). Through further measurements with $|e\rangle$ and $|o\rangle$ pumps to resolve the remaining ambiguity in the pump transverse modes, we can conclude that each JSI lobe is associated with a $\left(T_{p_1}, T_{p_2}, T_s, T_i\right)$ FWM process as labeled in Fig. 3: A (e, o, o, e), B (o, o, o, o), C (e, e, e, e), and D (e, o, e, o). To determine the center signal and idler wavelengths $(\lambda_s, \lambda_i)_j$ of the corresponding process, we fit each JSI lobe with a Gaussian function giving: $(680.7, 568.1)_A$ nm, $(678.7, 570.0)_B$ nm, $(677.2, 571.6)_C$ nm, and $(675.3, 573.3)_D$ nm. Remarkably, this characterization is also possible in real time (see Visualization 1 and Visualization 2), similar to Ref. [31] with free-space nonlinear crystals. Supplement 1 provides more information on the characterization efficiency and the relative intensities of the JSI lobes and their relation to the transverse-mode overlap integral O_j.

This characterization capability is instrumental in assessing the degree of spectral overlap among different FWM processes, which is essential for creating transverse-mode entanglement as we investigate in Section 4.2. The FWM processes are spectrally separated in the JSI due to different phase matching conditions and effective refractive indices of transverse modes, as explained in Section 2. Consequently, this means that the quantum state of a signal–idler photon pair expressed in the transverse-spectral-mode basis, $|\psi_{si}\rangle = \sum_j \int \mathrm{d}\lambda_s\, d\lambda_i\, c_j |T_s T_i, \lambda_s \lambda_i\rangle_j$ where j denotes a FWM process, becomes a mixed state in the transverse-mode basis with the spectral DOF is traced out, i.e., a reduced density matrix, $\rho_{si}^T = \mathrm{tr}_\lambda(\rho_{si}) = \sum_j C_j |T_s T_i\rangle_j \langle T_s T_i|_j$.

We now turn our attention to the processes B and C. We discovered that in order to explain the spectral separation between B and C, apparent in Fig. 3(c) and consistently observed in previous studies [54,55], a new correction parameter called parity birefringence dispersion δ needs to be introduced. Without such correction, the numerical simulation may incorrectly predict the two FWM processes to completely overlap in JSI [see Fig. 4(a)], which is instrumental for enabling transverse-mode entanglement [40,54–56]. For simplicity, here we assume that δ is a constant describing the difference between the signal and the idler parity birefringences, i.e., $\delta = \Delta_s^p - \Delta_i^p$. With numerical simulation, we vary δ and observe the change in JSI, as shown in Fig. 4. We find the non-zero dispersion of $\delta \sim 3 \times 10^{-5}$ [see Fig. 4(c)] best explains the experimental results presented in Fig. 3(c). Although δ is an order of magnitude smaller than Δ^p ($\sim 10^{-4}$), it contributes significantly to the spectral distinguishability between B and C processes, as shown in Fig. 4. The remaining discrepancies between the experimental data and numerical simulation arise due to imperfect estimation of the fiber parameters. Therefore, more accurate analysis using a full genetic algorithm calculation [10,11] along with precise

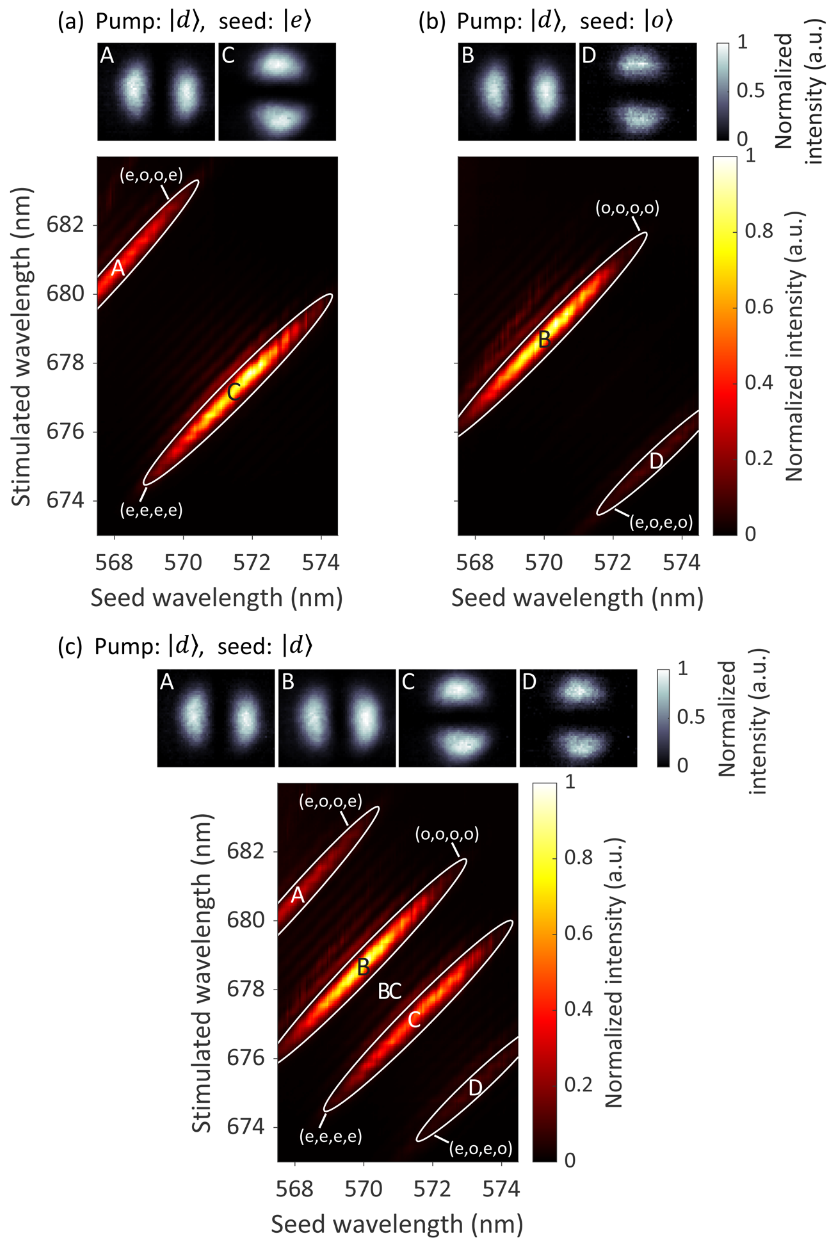

Fig. 3. Transverse-mode images (top subpanels) of the stimulated signal and JSI plots (bottom subpanel) of the FWM processes for different seed transverse modes, (a) $|e\rangle$, (b) $|o\rangle$, and (c) $|d\rangle$. The pump transverse mode is fixed to $|d\rangle$. Each FWM process (A–D) with transverse modes $(T_{p_1}, T_{p_2}, T_s, T_i)$ is specified with a solid $1/e^3$ two-dimensional Gaussian fit contour. The transverse mode images are captured with camera exposure times of (a,b) 200 ms and (c) 400 ms at the JSI peaks with narrow spectral filters on the stimulated signal to block other FWM contributions. The intensities of all the transverse mode images and JSI plots are normalized to one. See Visualization 1 and Visualization 2 for a real-time movie and an animated version of this data.

measurement of δ as a function of wavelength may help improve the agreement.

4.2. Transverse-Mode Quantum State Estimation from Transverse-Mode-Resolved JSIs

Building upon the characterization results described in Section 4.1, we apply stimulated emission to characterize a fiber source that generates photon pairs with partial transverse-mode entanglement. This characterization allows us to numerically estimate the quantum state of the photon pairs created in the transverse-mode basis. Through this process, we identify potential factors that can degrade the transverse-mode entanglement and find ways to optimize the source accordingly.

To create a maximally entangled transverse-mode Bell state in our system [54,55], $|\psi_{si}\rangle = (|e_s e_i\rangle + |o_s o_i\rangle)/\sqrt{2}$, indistinguishabilities between $|e_s e_i\rangle$ and $|o_s o_i\rangle$ in all other degrees of freedom are necessary, i.e., $C_{ee} = mC_{oo}$ [see Eq. (3)], where m is a constant. Consequently, the JSIs [Eq. (4)] need to satisfy the following overlap condition at the desired frequencies, ω_s and ω_i: $|f_{ee}(\omega_s, \omega_i)|^2 = |f_{oo}(\omega_s, \omega_i)|^2$. For this, we employ a shorter cross-spliced PMF (2.5 cm × 2, HB800C) with the same experimental setup used in Section 3. The smaller the fiber length L, the wider the spectral bandwidth of the phase-matching function

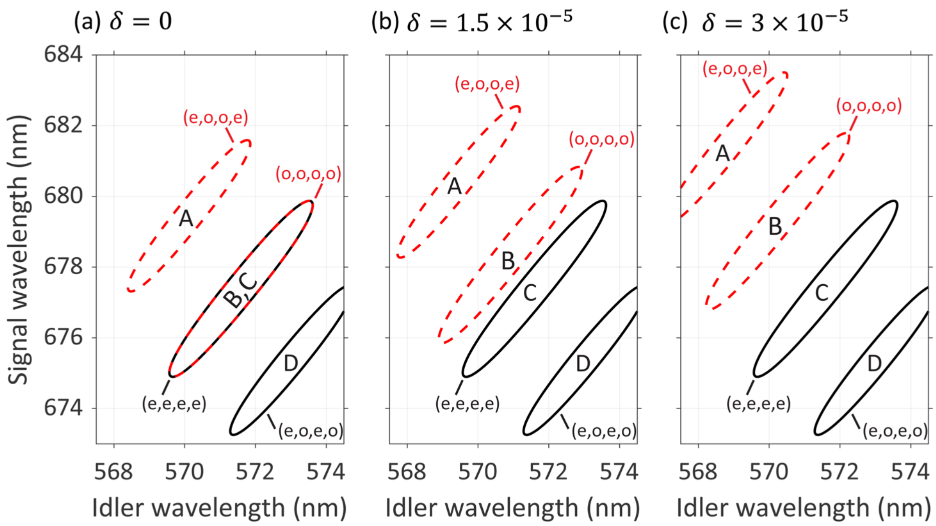

Fig. 4. Numerically simulated JSI plots for varying parity birefringence dispersion, δ: (a) 0; (b) 1.5×10^{-5}; and (c) 3×10^{-5}. The solid and dashed $1/e^3$ contours correspond to the SFWM processes labeled (A–D) and $(T_{p_1}, T_{p_2}, T_s, T_i)$. Increasing the parity birefringence dispersion δ increases the spectral separation between C (e,e,e,e) and B (o,o,o,o) by translating A (e,o,o,e) and B (o,o,o,o) (dashed) toward the top left. The pump is fixed to $|d\rangle$.

$\phi(\omega_s, \omega_i)$ (see Section 2.3) and thus the more spectral overlap arise along the anti-diagonal direction in the JSI. Cross-splicing, where we fusion splice two 2.5 cm-long PMFs such that the second fiber's slow axis is aligned along the first fiber's fast axis, helps compensate for temporal walk-off between the $|e\rangle$ and $|o\rangle$ modes [57].

With a shorter fiber for spectral indistinguishability and cross-splicing for temporal indistinguishability, we measure transverse-mode-resolved JSIs as in Section 3. To identify the FWM processes, similar to Fig. 3, we conduct a series of measurements with five different pump-seed transverse-mode combinations (*e-e*, *o-o*, *d-e*, *d-o*, and *d-a*). Figure 5(a) shows the measured JSI with the pump in $|d\rangle$ and the seed in $|a\rangle$, where we have labeled the spectral peaks with the associated transverse modes $(T_{p_1}, T_{p_2}, T_s, T_i)$ and FWM processes as before. The solid curves in Fig. 5(a) again represent the $1/e^2$ contours of the two-dimensional Gaussian curve fittings (goodness of fit $R^2 \approx 0.9$). The B and C contours exhibit some spectral overlap, promising some transverse-mode entanglement at the intersection. Compared with Figs. 3(a)–3(c), in Fig. 5(a), the four processes A, B, C, and D are positioned much closer despite considering the fiber length change effect—A and D are located fully inside B and C. Here, we attribute this deviation to the difference in fiber parameters. Even for the same type of fiber, HB800C, the fiber parameters can vary spool to spool, which may result in different FWM peak positions. Here, given that the fibers used for Figs. 3(a)–3(c) and 5(a) are from different spools, we identify that this shorter PMF likely has a smaller parity birefringence $\Delta^p \sim 1 \times 10^{-4}$ compared with that used in Section 4.1.

Before estimating the signal–idler quantum state with our stimulated emission approach, for reference, we measure the state using a conventional transverse-mode QST [15]. Specifically, we project the signal–idler transverse-mode states into six mutually unbiased measurement basis states (e, o, d, a, r, l) and conduct 36 coincidence measurements $(ee, eo, \ldots, lr, ll)$ [15,38,55,58–60] by installing an additional SLM, single-mode fibers, single-photon detectors, and a coincidence counter in the detection part of the setup in Fig. 2 (see Supplement 1 for more details). Figure 5(b) shows the measured density matrix ρ_{QST} with partial transverse-mode entanglement quantified by concurrence = 0.27 ± 0.03. It has a fidelity, or closeness, to the target Bell state of 0.48 ± 0.02 and a purity of 0.52 ± 0.01. As with typical quantum state tomography results, we can only roughly ascribe the low concurrence, fidelity, and purity to low $|ee\rangle\langle oo|$ and $|oo\rangle\langle ee|$ off-diagonal cross terms and non-zero $|oe\rangle\langle oe|$ and $|eo\rangle\langle eo|$ on-diagonal components each describing the coherence and purity of $|ee\rangle$ and $|oo\rangle$ states, respectively. We can hypothesize the origins of such contributions, but it will be challenging to trace and verify them experimentally without conducting additional measurements. The errors presented here are computed from 10^2 randomly sampled density matrices assuming Poissonian noise in the coincidence counts for QST.

To compare with the QST, we estimate the transverse-mode density matrix ρ_{SE} from the transverse-mode-resolved JSI, which can provide additional information about the sources of low concurrence, fidelity, and purity. We start the estimation procedure by characterizing the transverse-mode density matrix $\rho_{tot}(\lambda_s, \lambda_i)$ $(\rho_{tot}(\omega_s, \omega_i))$ in the signal–idler wavelength (frequency) space. Using spectral decomposition [61], the full density matrix at given signal and idler wavelengths can be represented as a linear combination of density matrices ρ_j as $\rho_{tot}(\lambda_s, \lambda_i) = \sum_j m_j \rho_j(\lambda_s, \lambda_i)$, where each $\rho_j = |\psi_j\rangle\langle\psi_j|$ describes a pure quantum state $|\psi_j\rangle$ of a FWM process j satisfying the normalization condition $\sum_j m_j = 1$ with $m_j \geq 0$. For example, ρ_B, ρ_C, and $\rho_{B\cap C}$ each represents a pure signal–idler state within the boundary of the process B, C, and the intersection of B and C, respectively, where $|\psi_B\rangle = C_B \otimes |oo\rangle_B$, $|\psi_C\rangle = C_C \otimes |ee\rangle_C$, and $|\psi_{B\cap C}\rangle = C_C \otimes |ee\rangle_C + C_B \otimes |oo\rangle_B$. In general, if N-FWM processes exist, there will be $2^N - 1$ binary combinations of ρ_j that specify whether a given signal–idler wavelength coordinate lies inside or outside of a certain FWM process. Representing each FWM process with a two-dimensional Gaussian fitting function as shown in Fig. 5(a) simplifies the density matrix calculation at a given signal–idler wavelength domain and thus the estimation procedure. Then, we integrate all these pointwise density matrices in the given signal–idler spectral range

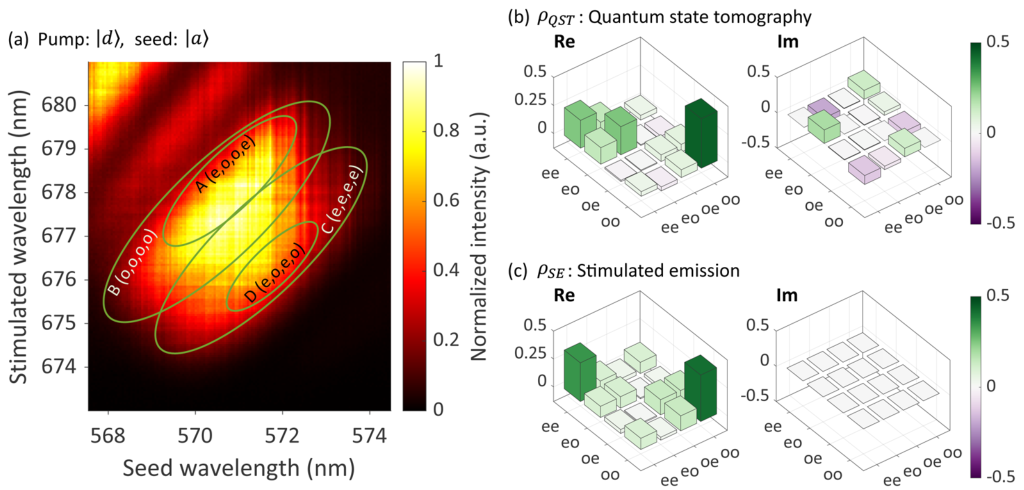

Fig. 5. (a) The JSI plot of a (2.5 cm × 2) cross-spliced PMF with the pump in $|d\rangle$ and the seed in $|a\rangle$. The $1/e^2$ contours (solid lines) show the two-dimensional Gaussian fits for FWM processes $(T_{p_1}, T_{p_2}, T_s, T_i)$. (b),(c) Density matrices describing the transverse-mode quantum state of the photon pairs created: (b) ρ_{QST} measured with a transverse-mode QST and (c) ρ_{SE} estimated from the stimulated-emission measurements in (a). The fidelity F between the two density matrices is 0.73, which increases to 0.85 when disregarding the phase.

experimentally defined by interference filters, thereby producing a single transverse-mode density matrix we name ρ_{SE}. In other words, ρ_{SE} is a reduced density matrix ρ_{tot}^{T} in the transverse-mode domain, where the spectral DOF is traced out: $\rho_{SE} = \rho_{tot}^{T} = tr_{\lambda}(\rho_{tot}(\lambda_s, \lambda_i)) = \int d\lambda_s\, d\lambda_i\, \rho_{tot}(\lambda_s, \lambda_i)$.

Figure 5(c) shows the stimulated-emission estimated density matrix ρ_{SE} using this calculation accounting for the interference filters used in the QST measurement (the full range shown in Fig. 5(a); $\lambda_i = [567.5, 574.5]$ nm, $\lambda_s = [673.0, 681.0]$ nm). Here ρ_{SE} exhibits concurrence = 0.00, Bell fidelity = 0.48, and purity = 0.40. Except for the relative amplitude of $|ee\rangle\langle ee|$ and $|eo\rangle\langle eo|$ elements, overall, ρ_{SE} shows a similar trend as the quantum state tomography result, ρ_{QST}—high $|ee\rangle\langle ee|$ and $|oo\rangle\langle oo|$, non-zero $|ee\rangle\langle oo|$ and $|oo\rangle\langle ee|$ coherent interaction elements, and other residual elements. Quantitatively, the fidelity F that describes the degree of similarity between the QST and stimulated-emission estimated states is $F(\rho_{QST}, \rho_{SE}) = 0.73$. ρ_{SE} provides a closer estimation if the phase information can be ignored, i.e., $F(|\rho_{QST}|, \rho_{SE}) = 0.85$. This is related to the current phase measurement limitation of our method as shall be discussed later in Section 4.3.

Despite the remaining discrepancies, ρ_{SE} can still provide sufficient information to deduce potential factors leading to low transverse-mode entanglement, namely, the presence of spectral distinguishabilities among the FWM processes. Within the given spectral window in Fig. 5(a), imperfect spectral overlap between the processes B and C can be observed, as well as the presence of other processes A and D. Based on the previous discussions, we can realize that in the transverse-mode basis, spectral overlap between the two processes gives coherence (off-diagonal components in the density matrix), whereas spectral separation gives incoherence (no off-diagonals, leading to a mixed state). Therefore, between $|oo\rangle$ (B) and $|ee\rangle$ (C), we can logically predict that the density matrix will have slight off-diagonal coherence from the B–C overlap in the JSI, as well as the mostly on-diagonal incoherence from the remaining spectrally non-overlapping regions. Similarly, examining the JSI plot in Fig. 5(a), we can infer that while $|eo\rangle$ (D) and $|oe\rangle$ (A) will not have off-diagonal elements, they will have non-zero off-diagonal values with $|oo\rangle$ (B) and $|ee\rangle$ (C), respectively [see Fig. 5(c)]. Ultimately, all these factors contribute to low transverse-mode entanglement. As such, the stimulated-emission method can help probe spectral distinguishabilities that are challenging to assess solely based on the transverse-mode QST result.

Considering the spectral origin, we may now think about tailored strategies to optimize the source for higher transverse-mode entanglement, that is, lowering the spectral distinguishability. In principle, we can do so by choosing a narrower spectral window that focuses on the B–C intersection area at the cost of reduced counts. Since we can choose an arbitrary spectral window when calculating ρ_{SE}, we can easily simulate to determine the optimal filtering strategy. For example, making a 1.5 cm × 2 fiber source out of the Section 4.1 fiber and using a square-shaped 1 nm-wide spectral window centered at B–C intersection can produce a photon-pair state with concurrence = 0.82, Bell fidelity = 0.91, and purity = 0.84. More fundamentally, we may engineer the phase-matching [62] to increase the B–C overlap while decreasing the A and D contributions.

4.3. Discussion on Possible Improvements

The aforementioned difference in quantitative measures (concurrence, Bell fidelity, and purity) between ρ_{QST} and ρ_{SE} can be explained by the following assumptions made in the calculation, which may improve with adequate treatments. First, we assume a Gaussian phase-matching function instead of the more accurate sinc (degenerate pumps) and complex error functions (non-degenerate pumps) described in Section 2.3. A Gaussian function can underestimate the spectral overlap that may originate from the tails of the sinc and non-degenerate pump functions [44], reducing the overall entanglement. As a resolution, we may fit each FWM process with an accurate phase-matching function model accounting for the pump degeneracy (B, C: degenerate, A, D: non-degenerate). Alternatively, we may directly use a non-fitted raw JSI data that could be measured by exciting only one FWM process at a time using a precise transverse-mode control. Second, we assume a flat JSP for all the FWM processes involved. This lack of phase information can explain why the imaginary part of the ρ_{SE} is zero even though that of the ρ_{QST} is not. This can be addressed by measuring the JSP experimentally utilizing phase-sensitive interference effects as in Refs. [1,28,63,64]. The measured JSP will include information about the relative phase of each FWM process through complex-valued $c_j \propto f_j \propto e^{i(JSP)}$ [see Eq. (3) and Supplement 1 for more details]. Third, we assume we have accounted for all the FWM processes within the spectral range. As shown in the upper-left corner of Fig. 5(a), there exists a signature of a stimulated signal that may be associated with FWM processes (outside A–D) involving $|g\rangle$ modes caused by imperfect spatial-mode control. Although the quantum state tomography [Fig. 5(b)] should be able to filter out the $|g\rangle$-mode photon pairs sufficiently [23], imperfections may still contribute to errors in measuring ρ_{QST}. Thus, conducting a qutrit ($|g\rangle$, $|e\rangle$, $|o\rangle$) QST [59] may help probe the full spatial dimension of the few-mode PMF used. As detailed below, stimulated-emission tomography [14,25,27,33] with sufficient spatiospectral control may also aid with faster acquisition for the larger numbers of measurements required for qutrit QST while maintaining accuracy. Lastly, we assume the distinguishabilities that can undermine the transverse-mode entanglement do not exist outside the spatial and spectral DOFs. Although the linear polarizers and a cross-spliced fiber are employed to compensate any residual polarization and temporal distinguishabilities in the system (the second PMF in the cross-spliced PMF corrects for polarization- and transverse-mode parity-dependent temporal walk-offs introduced in the first PMF [57]), there is a chance that some unaccounted distinguishabilities still remain. As a remedy, extending the technique to other DOFs, e.g., polarization and time-resolved characterization, may be helpful [14,65]. Alternatively, we may also consider a full frequency-resolved transverse-mode stimulated emission tomography, whose projection measurements naturally account for all possible distinguishabilities as well as the phases between different spatial modes. This may produce better estimation, albeit will lack the information on the source of distinguishability if it exists outside the spatial and spectral domains. In addition, the stimulated emission tomography may not capture parasitic noise processes present at the single-photon level, such as Raman scattering. Ultimately, all the resolutions presented here can lead to potential improvements in the numerical model used in previous works [10–12] to better predict the quantum state.

5. CONCLUSION

We have applied a stimulated-emission-based characterization technique to reveal the transverse-mode-frequency relation of photon pairs created from four-wave mixing processes in few-mode PMF. We measured the joint spectral intensities and transverse modes of the stimulated signal while controlling the pump and seed transverse modes and the seed wavelength. From these measurement results, we identified FWM processes predicted by theory and an additional parity birefringence dispersion parameter δ required to explain the spectral distinguishability between $|e_s e_i\rangle$ and $|o_s o_i\rangle$ photon-pair states. We demonstrated the efficiency of our technique by comparing with spontaneous measurements for imaging signal transverse modes. Leveraging the efficiency of stimulated-emission-based measurement, we demonstrated real-time imaging capability and investigated the quantum properties of a transverse-mode entangled photon-pair source. We illustrated how the transverse-mode quantum state of the photon pairs can be estimated from the spatiospectral measurements, specifically transverse-mode-resolved stimulated JSIs. The estimated density matrix ρ_{SE} showed qualitative agreement with that measured from a standard transverse-mode QST, ρ_{QST}. Estimating ρ_{SE} provided additional information on spectral distinguishability that can lead to low transverse-mode entanglement.

This stimulated-emission-based spatiospectral characterization technique may benefit from a possible extension to a spectrally resolved transverse-mode stimulated-emission tomography [14,25,27] and joint spectral phase measurement [1,28]. By allowing the diagnosis of potential causes of entanglement degradation originating from other degrees of freedom, this method may be utilized to create versatile fiber-based photon-pair sources with entanglement in frequency and transverse mode [54,55], as well as transverse-mode-frequency hybrid-entanglement [10]. We anticipate this stimulated-emission characterization technique may also be extended beyond few-mode optical fiber [56,66] to efficiently diagnose and optimize photon-pair sources in a variety of quantum systems with high dimensionality [67–71] and different degrees of freedom [14,16,72,73].

Funding. National Science Foundation (1806572, 1640968, 1839177, 2207822); U.S. Department of Energy (DE-SC0023167).

Acknowledgments. We thank Joel Carpenter for help with transverse-mode control using an SLM; Elizabeth Goldschmidt for help with aligning the CW dye laser; Oliver Wang and Xinan Chen for the initial experimental setup; Offir Cohen and Bin Fang for helpful discussions about density matrix error analysis; Xiao Liu, Daniel Shahar, and Siddharth Ramachandran for fruitful discussions about OAM modes; and Soho Shim for valuable discussions during the manuscript preparation.

Disclosures. The authors declare no conflicts of interest.

Data availability. Data underlying the results presented in this paper are not publicly available at this time but may be obtained from the authors upon reasonable request.

Supplemental document. See Supplement 1 for supporting content.

REFERENCES

1. K. Garay-Palmett, D. B. Kim, Y. Zhang, *et al.*, “Fiber-based photon-pair generation: tutorial,” J. Opt. Soc. Am. B **40**, 469–490 (2023).
2. A. Anwar, C. Perumangatt, F. Steinlechner, *et al.*, “Entangled photon-pair sources based on three-wave mixing in bulk crystals,” Rev. Sci. Instrum. **92**, 041101 (2021).
3. M. Krenn, M. Malik, M. Erhard, *et al.*, “Orbital angular momentum of photons and the entanglement of Laguerre–Gaussian modes,” Phil. Trans. R. Soc. A. **375**, 20150442 (2017).
4. A. E. Willner, “OAM light for communications,” Opt. Photonics News **32**, 34–41 (2021).
5. D. Halevi, B. Lubotzky, K. Sulimany, *et al.*, “High-dimensional quantum key distribution using orbital angular momentum of single photons from a colloidal quantum dot at room temperature,” Optica Quantum **2**, 351–357 (2024).
6. M. Hiekkamäki and R. Fickler, “High-dimensional two-photon interference effects in spatial modes,” Phys. Rev. Lett. **126**, 123601 (2021).
7. T. Gregory, P.-A. Moreau, E. Toninelli, *et al.*, “Imaging through noise with quantum illumination,” Sci. Adv. **6**, eaay2652 (2020).
8. R. S. Aspden, N. R. Gemmell, P. A. Morris, *et al.*, “Photon-sparse microscopy: visible light imaging using infrared illumination,” Optica **2**, 1049–1052 (2015).
9. P.-A. Moreau, E. Toninelli, T. Gregory, *et al.*, “Ghost imaging using optical correlations,” Laser Photonics Rev. **12**, 1700143 (2018).

10. D. Cruz-Delgado, R. Ramirez-Alarcon, E. Ortiz-Ricardo, *et al.*, "Fiber-based photon-pair source capable of hybrid entanglement in frequency and transverse mode, controllably scalable to higher dimensions," Sci. Rep. **6**, 1–9 (2016).
11. K. Garay-Palmett, D. Cruz-Delgado, F. Dominguez-Serna, *et al.*, "Photon-pair generation by intermodal spontaneous four-wave mixing in birefringent, weakly guiding optical fibers," Phys. Rev. A **93**, 033810 (2016).
12. D. Cruz-Delgado, J. Monroy-Ruz, A. M. Barragan, *et al.*, "Configurable spatiotemporal properties in a photon-pair source based on spontaneous four-wave mixing with multiple transverse modes," Opt. Lett. **39**, 3583–3586 (2014).
13. K. Zielnicki, K. Garay-Palmett, D. Cruz-Delgado, *et al.*, "Joint spectral characterization of photon-pair sources," J. Mod. Opt. **65**, 1141–1160 (2018).
14. B. Fang, M. Liscidini, J. Sipe, *et al.*, "Multidimensional characterization of an entangled photon-pair source via stimulated emission tomography," Opt. Express **24**, 10013–10019 (2016).
15. J. B. Altepeter, E. R. Jeffrey, and P. G. Kwiat, "Photonic state tomography," Adv. At., Mol., Opt. Phys. **52**, 105–159 (2005).
16. J. T. Barreiro, N. K. Langford, N. A. Peters, *et al.*, "Generation of hyperentangled photon pairs," Phys. Rev. Lett. **95**, 260501 (2005).
17. M. Rambach, M. Qaryan, M. Kewming, *et al.*, "Robust and efficient high-dimensional quantum state tomography," Phys. Rev. Lett. **126**, 100402 (2021).
18. F. Huszár and N. M. Houlsby, "Adaptive Bayesian quantum tomography," Phys. Rev. A **85**, 052120 (2012).
19. D. H. Mahler, L. A. Rozema, A. Darabi, *et al.*, "Adaptive quantum state tomography improves accuracy quadratically," Phys. Rev. Lett. **111**, 183601 (2013).
20. C. Ferrie, "Self-guided quantum tomography," Phys. Rev. Lett. **113**, 190404 (2014).
21. D. Gross, Y.-K. Liu, S. T. Flammia, *et al.*, "Quantum state tomography via compressed sensing," Phys. Rev. Lett. **105**, 150401 (2010).
22. F. Bouchard, D. Koutnỳ, F. Hufnagel, *et al.*, "Compressed sensing of twisted photons," Opt. Express **27**, 17426–17434 (2019).
23. F. Bouchard, N. H. Valencia, F. Brandt, *et al.*, "Measuring azimuthal and radial modes of photons," Opt. Express **26**, 31925–31941 (2018).
24. D. Zia, N. Dehghan, A. D'Errico, *et al.*, "Interferometric imaging of amplitude and phase of spatial biphoton states," Nat. Photonics **17**, 1009–1016 (2023).
25. M. Liscidini and J. Sipe, "Stimulated emission tomography," Phys. Rev. Lett. **111**, 193602 (2013).
26. B. Fang, O. Cohen, M. Liscidini, *et al.*, "Fast and highly resolved capture of the joint spectral density of photon pairs," Optica **1**, 281–284 (2014).
27. L. A. Rozema, C. Wang, D. H. Mahler, *et al.*, "Characterizing an entangled-photon source with classical detectors and measurements," Optica **2**, 430–433 (2015).
28. G. Thekkadath, B. Bell, R. Patel, *et al.*, "Measuring the joint spectral mode of photon pairs using intensity interferometry," Phys. Rev. Lett. **128**, 023601 (2022).
29. D. Caetano, M. Almeida, P. S. Ribeiro, *et al.*, "Conservation of orbital angular momentum in stimulated down-conversion," Phys. Rev. A **66**, 041801 (2002).
30. A. de Oliveira, G. Santos, N. R. da Silva, *et al.*, "Beyond conservation of orbital angular momentum in stimulated parametric down-conversion," Phys. Rev. Appl. **16**, 044019 (2021).
31. A. G. de Oliveira, M. F. Arruda, W. C. Soares, *et al.*, "Real-time phase conjugation of vector vortex beams," ACS Photonics **7**, 249–255 (2019).
32. Y. Xu, S. Choudhary, and R. W. Boyd, "Efficient measurement of the bi-photon spatial mode entanglement with stimulated emission tomography," arXiv (2024).
33. M. A. Ciampini, A. Geraldi, V. Cimini, *et al.*, "Stimulated emission tomography: beyond polarization," Opt. Lett. **44**, 41–44 (2019).
34. D. Kim, X. Hu, Y. Zhang, *et al.*, "Stimulated-emission-based characterization of optical fiber photon-pair source in frequency and transverse mode," in *Frontiers in Optics* (Optica Publishing Group, 2020), pp. JM6B–22.
35. J. Carpenter, B. C. Thomsen, and T. D. Wilkinson, "Degenerate mode-group division multiplexing," J. Lightwave Technol. **30**, 3946–3952 (2012).
36. J. Carpenter, B. J. Eggleton, and J. Schröder, "Complete spatiotemporal characterization and optical transfer matrix inversion of a 420 mode fiber," Opt. Lett. **41**, 5580–5583 (2016).
37. N. K. Fontaine, R. Ryf, H. Chen, *et al.*, "Laguerre-Gaussian mode sorter," Nat. Commun. **10**, 1–7 (2019).
38. A. Mair, A. Vaziri, G. Weihs, *et al.*, "Entanglement of the orbital angular momentum states of photons," Nature **412**, 313–316 (2001).
39. L.-T. Feng, M. Zhang, X. Xiong, *et al.*, "On-chip transverse-mode entangled photon pair source," npj Quantum Inf **5**, 2–7 (2019).
40. Ç. Ekici and M. S. Dinleyici, "Graded-index optical fiber transverse-spatial-mode entanglement," Phys. Rev. A **102**, 013702 (2020).
41. K. Sulimany and Y. Bromberg, "All-fiber source and sorter for multimode correlated photons," npj Quantum Inf **8**, 4–5 (2022).
42. C. L. Morrison, F. Graffitti, P. Barrow, *et al.*, "Frequency-bin entanglement from domain-engineered down-conversion," APL Photonics **7**, 1 (2022).
43. A. W. Snyder and J. D. Love, *Optical Waveguide Theory*, Vol. 175 (Chapman and Hall London, 1983).
44. K. Garay-Palmett, H. McGuinness, O. Cohen, *et al.*, "Photon pair-state preparation with tailored spectral properties by spontaneous four-wave mixing in photonic-crystal fiber," Opt. Express **15**, 14870–14886 (2007).
45. R. Boyd, *Nonlinear Optics* (Elsevier Science, 2020).
46. Q. Lin, F. Yaman, and G. P. Agrawal, "Photon-pair generation in optical fibers through four-wave mixing: role of Raman scattering and pump polarization," Phys. Rev. A **75**, 023803 (2007).
47. B. J. Smith, P. Mahou, O. Cohen, *et al.*, "Photon pair generation in birefringent optical fibers," Opt. Express **17**, 23589–23602 (2009).
48. K. Zielnicki, K. Garay-Palmett, R. Dirks, *et al.*, "Engineering of near-IR photon pairs to be factorable in space-time and entangled in polarization," Opt. Express **23**, 7894–7907 (2015).
49. B. Fang, O. Cohen, J. B. Moreno, *et al.*, "State engineering of photon pairs produced through dual-pump spontaneous four-wave mixing," Opt. Express **21**, 2707–2717 (2013).
50. Y. Zhang, R. Spiniolas, K. Shinbrough, *et al.*, "Dual-pump approach to photon-pair generation: demonstration of enhanced characterization and engineering capabilities," Opt. Express **27**, 19050–19061 (2019).
51. P. Boucher, H. Defienne, and S. Gigan, "Engineering spatial correlations of entangled photon pairs by pump beam shaping," Opt. Lett. **46**, 4200–4203 (2021).
52. J. A. Davis, D. M. Cottrell, J. Campos, *et al.*, "Encoding amplitude information onto phase-only filters," Appl. Opt. **38**, 5004–5013 (1999).
53. G. Labroille, B. Denolle, P. Jian, *et al.*, "Efficient and mode selective spatial mode multiplexer based on multi-plane light conversion," Opt. Express **22**, 15599–15607 (2014).
54. D. B. Kim, A. B. U'ren, K. Garay-Palmett, *et al.*, "Generating transverse-mode entanglement in optical fiber," in *Quantum Computing, Communication, and Simulation III*, Vol. 12446 (SPIE, 2023), pp. 174–176.
55. D. B. Kim, A. B. U'Ren, K. Garay-Palmett, *et al.*, "Towards transverse-mode entanglement generation in few-mode optical fiber," in *Quantum 2.0* (Optica Publishing Group, 2023), pp. QW2A–19.
56. A. Shamsshooli, C. Guo, F. Parmigiani, *et al.*, "Progress toward spatially-entangled photon-pair generation in a few-mode fiber," IEEE Photonics Technol. Lett. **33**, 864–867 (2021).
57. E. Meyer-Scott, V. Roy, J.-P. Bourgoin, *et al.*, "Generating polarization-entangled photon pairs using cross-spliced birefringent fibers," Opt. Express **21**, 6205–6212 (2013).
58. M. Agnew, J. Leach, M. McLaren, *et al.*, "Tomography of the quantum state of photons entangled in high dimensions," Phys. Rev. A **84**, 062101 (2011).
59. N. K. Langford, R. B. Dalton, M. D. Harvey, *et al.*, "Measuring entangled qutrits and their use for quantum bit commitment," Phys. Rev. Lett. **93**, 053601 (2004).

60. M. Hiekkamäki, S. Prabhakar, and R. Fickler, "Near-perfect measuring of full-field transverse-spatial modes of light," Opt. Express **27**, 31456–31464 (2019).
61. M. A. Nielsen and I. L. Chuang, *Quantum Computation and Quantum Information: 10th Anniversary Edition* (Cambridge University Press, 2010).
62. X. Liu, D. B. Kim, V. O. Lorenz, *et al.*, "Engineering joint spectral densities with orbital angular momentum states in optical fibers," in *CLEO: QELS_Fundamental Science* (Optica Publishing Group, 2022), pp. FF2J–1.
63. I. Hurvitz, A. Shukhin, L. Vidro, *et al.*, "Phase analysis of biphoton joint spectra by interference between different SPDC sources," Optica Quantum **2**, 358–364 (2024).
64. I. Jizan, B. Bell, L. G. Helt, *et al.*, "Phase-sensitive tomography of the joint spectral amplitude of photon pair sources," Opt. Lett. **41**, 4803–4806 (2016).
65. M. Plöschner, M. M. Morote, D. S. Dahl, *et al.*, "Spatial tomography of light resolved in time, spectrum, and polarisation," Nat. Commun. **13**, 4294 (2022).
66. S. Zhu, L. Cui, and X. Li, "Tailoring the spectro-temporal mode of photon pairs generated from interspatial-mode four-wave mixing," Opt. Lett. **49**, 3536–3539 (2024).
67. N. Bozinovic, Y. Yue, Y. Ren, *et al.*, "Terabit-scale orbital angular momentum mode division multiplexing in fibers," Science **340**, 1545–1548 (2013).
68. S. Ramachandran, P. Gregg, P. Kristensen, *et al.*, "On the scalability of ring fiber designs for OAM multiplexing," Opt. Express **23**, 3721–3730 (2015).
69. H. Defienne, M. Barbieri, I. A. Walmsley, *et al.*, "Two-photon quantum walk in a multimode fiber," Sci. Adv. **2**, e1501054 (2016).
70. D. I. Shahar, X. Liu, D. B. Kim, *et al.*, "Photon pair generation in oam modes at 780 and 1550 nm via spontaneous intermodal four wave mixing," in *CLEO: Fundamental Science* (Optica Publishing Group, 2023), pp. FF1L–5.
71. T. Onodera, M. M. Stein, B. A. Ash, *et al.*, "Scaling on-chip photonic neural processors using arbitrarily programmable wave propagation," arXiv (2024).
72. L. Serino, W. Ridder, A. Bhattacharjee, *et al.*, "Orchestrating time and color: a programmable source of high-dimensional entanglement," Optica Quantum **2**, 339–345 (2024).
73. F. Presutti, L. G. Wright, S.-Y. Ma, *et al.*, "Highly multimode visible squeezed light with programmable spectral correlations through broadband up-conversion," arXiv (2024).